

Received 13 November 2023, accepted 27 December 2023, date of publication 1 January 2024, date of current version 12 January 2024.

Digital Object Identifier 10.1109/ACCESS.2023.3348551

APPLIED RESEARCH

An Aperture-Coupled-Cross-Resonator FSS Based Spatial Filtering Patch Antenna Array

YE LI^{1,2}, XURAN NIE³, XINMI YANG^{4,5}, (Member, IEEE),
CHANGRONG LIU³, (Member, IEEE), XIANQI LIN^{4,5}, (Senior Member, IEEE),
AND KEMENG HUANG⁶

¹CCTEG Changzhou Research Institute, Changzhou 213015, China

²Tiandi (Changzhou) Automation Company Ltd., Changzhou 213015, China

³School of Electronics and Information Engineering, Soochow University, Suzhou 215006, China

⁴Yangtze Delta Region Institute (Huzhou), University of Electronic Science and Technology of China, Huzhou 313001, China

⁵School of Electronic Engineering, University of Electronic Science and Technology of China, Chengdu 611731, China

⁶Wutong Holding Group Company Ltd., Suzhou 215006, China

Corresponding author: Xinmi Yang (yxm_1@163.com)


This work was supported in part by the National Natural Science Foundation of China under Grant 61871280, Grant 61372012, and Grant 61671315; and in part by Tiandi Technology Company Ltd., Technology Innovation and Entrepreneurship Foundation, under Grant 2023-TD-ZD005-001.

ABSTRACT The employment of Massive MIMO technology in 5G communication results in a large number of RF channels in the base station. Therefore, the base station will suffer from the huge burden of equipping discrete bandpass filters under the traditional filtering strategy. An alternative filtering strategy called spatial filtering characterizes direct covering frequency selective surface (FSS) on multi-channel antenna array of base station and is expected to greatly relax the need for discrete bandpass filters. An aperture-coupled-cross-resonator (ACCR) FSS based spatial filtering scheme is investigated in this study. A low-profile spatial filtering patch array (LPSFPA) with thickness of $0.07\lambda_0$ and operating around 3.6GHz is constructed by placing an asymmetrical ACCR FSS tightly upon a patch antenna array with a half-period lateral shift. A good out-of-band suppression at both band-edges and enhanced in-band impedance bandwidth are achieved when the main beam is scanned with an elevation angle range of 0° to 30° and arbitrary azimuth angle. To verify the design, a finite LPSFPA sample whose main beam can be directed to $\theta_b = 0^\circ, 15^\circ$ and 30° in E plane by different phasing and power-dividing networks is fabricated and tested. The measured results show that the fabricated LPSFPA sample is superior to the ordinary radiation patch array without the ACCR FSS in terms of both the impedance bandwidth and out-of-band suppression for various main beam directions. For the normal-beam case, the measured -10 dB impedance bandwidth is from 3.6-3.8 GHz; the measured out-of-band suppression level of peak realized gain is more than 19 dB in the lower band-edge from 3.2-3.5 GHz and 17 dB in the upper band-edge from 3.9-4.2 GHz. The proposed spatial filtering scheme has no negative influence on the radiation performance of the radiation patch array.

INDEX TERMS Aperture-coupled-cross-resonators frequency selective surface (ACCR FSS), spatial filtering, patch antenna array.

I. INTRODUCTION

As an important method to improve spectrum utilization and channel capacity of communication systems, Massive MIMO technology is being applied over a wider range with

The associate editor coordinating the review of this manuscript and approving it for publication was Sandra Costanzo .

the popularization of 5G communication. However, as the number of RF channels in Massive MIMO communication systems increases significantly compared to previous generations of communication systems, the burden of RF front-end filtering also increases for Massive MIMO base stations. The traditional filtering solution for base station is to independently cascade a certain number of RF bandpass filters

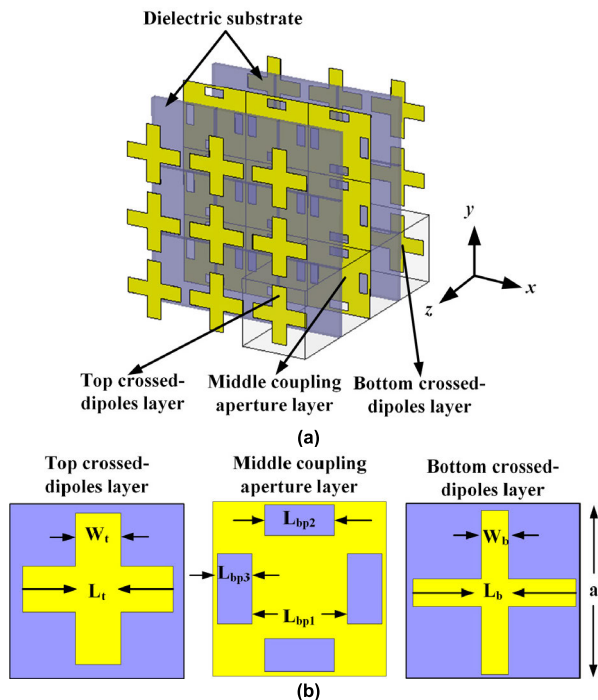


FIGURE 1. Geometry of ACCR FSS. (a) Overall view. (b) Element view for each metallic layer.

for each RF channel. The number of RF filters for Massive MIMO base station will become very large with this solution, which is rather unfavorable for design requirements such as low weight, small volume and low cost. In this background, many new filtering schemes that can effectively relax the need of discrete bandpass filters while maintaining good roll-off on both sides of passband for base stations have been proposed recently. The most direct and effective way is to integrate RF filters with radiator or feed structure of antenna to form a so-called filtering antenna. Early research on filtering antenna focused on direct co-designing of separated and neighboring filter and antenna [1], [2], [3], [4], [5]. Later, design of filtering antenna by considering antenna as both radiator and filtering resonator was proposed [6], [7], [8], [9]. In [10], [11], [12], [13], [14], [15], and [16], designs of filtering antennas without extra circuit were introduced to reduce structure volume and insertion loss. Metasurface technology was also employed in developing filtering antennas to achieve a great out-of-band suppression [17], [18]. However, most filtering antenna schemes developed to date were dedicated to single antenna element and not been investigated with regard to array response and beam scanning performance. This makes these filtering antenna schemes not practical in being applied to massive MIMO arrays, since mutual coupling in arrays will lead to deterioration of the original filtering performance. In view of this, approach of spatial filtering antenna array (SFAA) based on frequency selective surfaces (FSS) has been proposed for filtering the entire antenna array in recent years. The SFAA approach has the advantage of no change of radiator and feed structures when compared with

the filtering antenna schemes. Early research on SFAA was carried out by placing bandpass FSS directly upon patch antenna array to achieve a filtering characteristic [19], [20]. However, owing to the weak out-of-band suppression capability and poor angular stability of the FSS employed, the filtering performance in [19] and [20] are far worse than those of the traditional filtering methods. In later researches on SFAA, multilayer miniaturized-element FSS (MEFSS) [21] was utilized to further improve filtering performance [22], [23]. While an improved filtering and scanning performance was achieved in [22] and [23], the improvement of the out-of-band suppression is still not sufficient and the multilayer cascading nature of the MEFSS structure makes the overall pass band insertion loss large. The angular stability of the MEFSS-based designs is also poor. Recently, a single-layer FSS was designed based on conformational space annealing (CSA) algorithm and combined with a 5G antenna array [24]. The resulting SFAA has advantages such as low in-band insertion loss and stable angular-response.

In this study, an alternative spatial filtering strategy is proposed by employing bandpass FSS composed of aperture-coupled-cross-resonators (ACCR). It has been found that when an appropriately designed ACCR FSS is closely placed upon a patch antenna array, the resultant compound array achieves an enhanced bandwidth and improved filtering characteristic without a significant increase in insertion loss and distortion of radiation pattern. The rest of this paper is organized as follows. Section II describes the design of ACCR FSS and a preliminary design of spatial filtering patch array (SFPA). In Section III, a low-profile design of spatial filtering patch array (LPSFPA) is presented and discussed. Section IV provides the beam-scanning properties of the LPSFPA. Experimental verification is given in Section V. Finally, a conclusion is drawn in Section VI.

II. ACCR FSS AND PRELIMINARY DESIGN OF SPATIAL FILTERING PATCH ARRAY

The ACCR FSS was originally proposed in [25] and [26] in the millimeter-wave band. It provides a highly selective narrow bandpass response for plane wave and has good stability with respect to both incident angle and polarization. Figure 1 illustrates the geometry of ACCR FSS, which is composed of three metallic layers separated by two dielectric substrates. In this work, the two substrates share the same permittivity, loss tangent and thickness, which are $\epsilon_{r1} = 3$, $\tan\delta_1 = 0.002$ and $d = 1.5\text{mm}$, respectively. The middle metallic layer is a coupling aperture array while the top and bottom metallic layers are the same crossed-dipoles arrays. Under normal plane wave incidence, the voltage peaks are mainly distributed around the ends of the crossed-dipoles, which leads to an electrical coupling path through the middle coupling aperture layer. Also, the current peaks are mainly distributed around the center of the crossed-dipoles, which leads to a magnetic coupling through the middle coupling aperture layer. Hence it is convenient to change coupling properties by changing the size and position of apertures

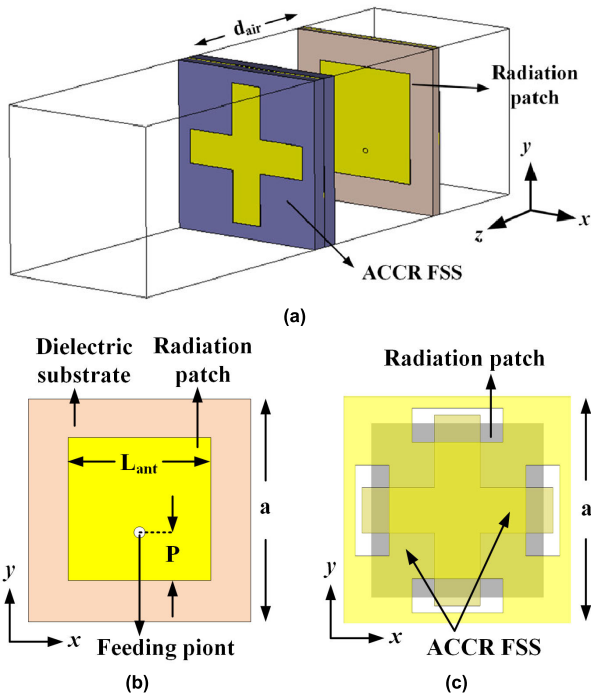


FIGURE 2. Element geometry of the preliminary design of SFPA. (a) 3-D view. (b) Front view of radiation patch. (c) Front view of ACCR FSS element showing the relative position of the radiation patch.

in middle layer to achieve a desired second-order bandpass response with two out-of-band transmission zeros. In general, for both TE and TM polarization, the ACCR FSS structure has a stable bandpass response in the elevation angle range of 0° to 30° with arbitrary azimuth angle.

An ACCR FSS is designed in a band around 3.6GHz. Table 1 lists the geometrical parameters and Fig. 3 presents the band-pass performance (blue lines) of the ACCR FSS. The reflection and transmission coefficients shown in Fig. 3 is obtained by simulating a single element surrounded by unit cell boundary and excited by normally incident plane wave via Floquet port in CST Microwave Studio. It can be seen that the FSS has a 3dB bandwidth from 3.44GHz to 3.58GHz and two transmission zeros at 3.22GHz and 4.24GHz, together with maximum in-band insertion loss 0.71dB at 3.5GHz. It should be noted that in order to obtain better in-band matching, the original two transmission poles of ACCR FSS are adjusted to be very close to each other. Hence the designed ACCR FSS appears to have only first-order bandpass characteristic.

An infinitely large radiation patch array is also designed in approximately the same frequency band as that of the ACCR FSS. Each array element is fed by $50\text{-}\Omega$ coaxial probe as illustrated in Fig. 2(b). The permittivity, loss tangent and thickness of the antenna substrate are $\epsilon_{r2} = 3.66$, $\tan\delta_2 = 0.007$ and $t = 0.762\text{mm}$, respectively. The geometrical parameters of the radiation patch array are also listed in Table 1. Note that the radiation patch array shares the same in-plane periodicity along both x and y directions as that of the ACCR FSS. The reflection and transmission coefficients of the radiation patch

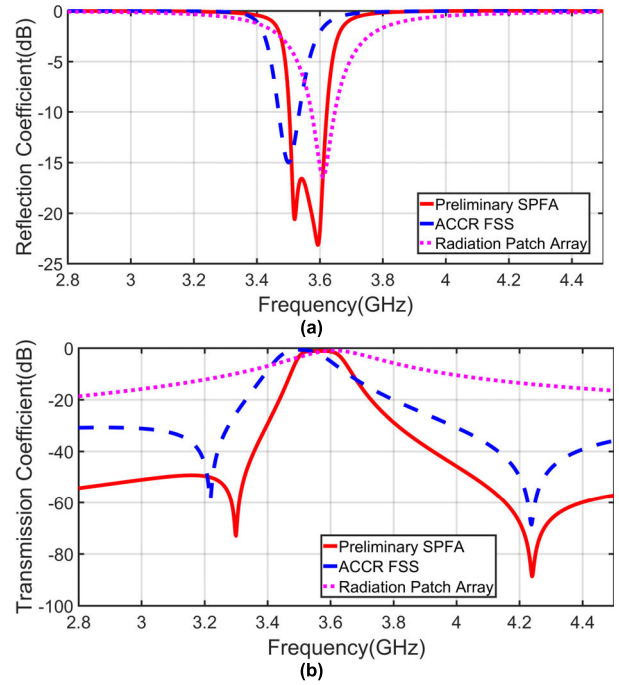


FIGURE 3. Band-pass performance comparison for the preliminary design of SFPA, ACCR FSS and conventional radiation patch array. (a) Reflection coefficient (b) Transmission coefficient.

TABLE 1. Geometrical dimensions of the ACCR FSS and the radiation patch array for preliminary SFPA design.

Parameters	Value
L_t	26.5mm
L_b	26.5mm
W_t	6.5mm
W_b	6.5mm
a	32mm
L_{bp1}	24.3mm
L_{bp2}	9.4mm
L_{bp3}	3.65mm
a	32mm
L_{ant}	21.2mm
P	5.1mm

array are shown by purple lines in Fig. 3. Note these two quantities are with respect to the reflected wave in the coaxial line and the plane wave emitted by the array when all antenna elements are excited at coaxial feeds with equal-amplitude and equal-phase. They are obtained by applying in-phase unit cell boundary condition around a single patch element, placing Floquet port in front of the element and activating the coaxial feed by waveguide port in CST Microwave Studio. Apparently, the radiation patch array alone has poor filtering property.

A preliminary design of spatial filtering patch array (SFPA), which is shown in Fig 2, is formed by simply placing the designed ACCR FSS upon the radiation patch array with a distance of $d_{air} = 21\text{mm}$, which is approximately a quarter-wavelength at 3.6GHz. Note the radiation patch is right behind the crossed-dipoles of the FSS in this SFPA design, as shown in Fig. 2(c). The reflection and transmission

coefficients of the infinitely large SFPA structure are obtained via CST Microwave Studio using the same simulation configuration as that used for the radiation patch array alone and are shown by red curves in Fig. 3. It can be seen that the transition between the pass and stop bands of the SFPA is much steeper than that of the radiation patch array alone. Moreover, it appears that the introduction of the ACCR FSS produced a very small additional insertion loss. The maximum in-band insertion loss of the SFPA is 1.14dB within its 3dB bandwidth from 3.5GHz to 3.63GHz. Correspondingly, the radiation patch array alone has a maximum in-band insertion loss of 0.95dB within its 3dB bandwidth from 3.48GHz to 3.74GHz. In fact, owing to the large separation distance and hence the negligible coupling between the radiation patch array and the ACCR FSS, the 2-port network response of the SFPA is simply the cascading of the radiation antenna array, the quarter-wavelength air space and the ACCR FSS alone. Nevertheless, although the preliminary SFPA design exhibits good spatial filtering performance, it is impractical owing to its large overall thickness.

III. LOW-PROFILE DESIGN OF SPATIAL FILTERING PATCH ARRAY

As discussed in the previous section, it is necessary to reduce the distance between the ACCR FSS and the radiation patch array to obtain a sufficiently low overall profile. However, directly reducing this distance causes serious deterioration in the filtering performance. As shown in Fig 4, the radiated field of the patch array gradually changes from induced near-field to far-field with the increase of the distance from the array surface. At the position of a quarter-wavelength distance from the array, the radiated electromagnetic wave behaves like a plane wave as that in the far-field region, indicating that a quarter-wavelength distance between the ACCR FSS and the radiation patch leads to weakening direct coupling. If the FSS is placed very close to the array surface, the near-field coupling between the radiation patch and the ACCR FSS is strong and the responses of the two crossed-dipoles arrays become asymmetrical, which makes the filtering performance of the ACCR FSS deviate from that of the free-standing case.

This section presents a design of a low-profile spatial filtering patch array (LPSFPA). For this design, in addition to the decreasing of patch-FSS-spacing (d_{air}), two approaches have been taken to avoid performance deterioration. First, the ACCR FSS is translated by half of periodic length along the x -axis with respect to the radiation patch array. It can be seen from Fig.5(a) that if this half-periodicity lateral offset is made, the crossed-dipoles array facing the radiation patch array can be immersed in an approximately-uniform field environment as they do when the ACCR FSS is situated in the far-field region of radiation patch array (Fig.5(b)). Second, asymmetrical physical dimensions are assigned to the two crossed-dipoles arrays to maintain a symmetrical response. The resulting overall view of the LPSFPA element is shown in Fig. 6(a). Note that the crossed-dipoles on the two sides

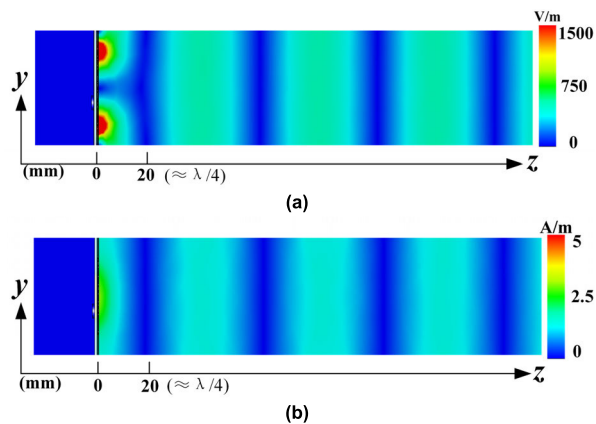


FIGURE 4. Side view of magnitude distribution of (a) electric and (b) magnetic field in the space above the radiation patch array. Only area for a single radiation patch element is shown here and the involved observation frequency is 3.7GHz.

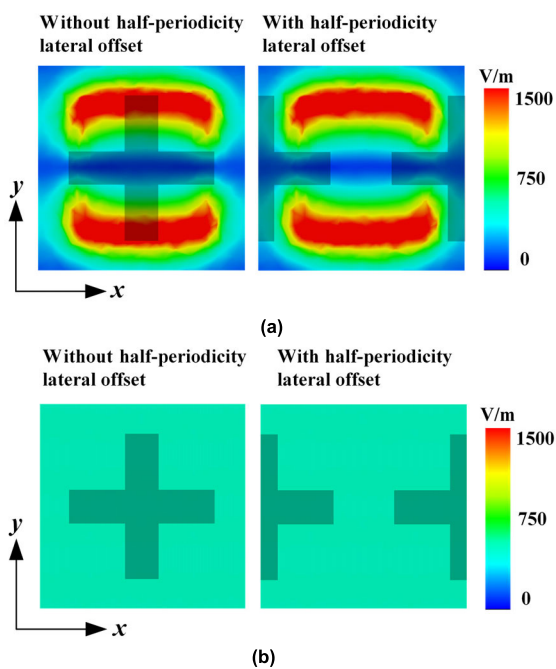


FIGURE 5. Front view of magnitude distribution of electric field at a distance of (a) $z = 2$ mm (near-field region) and (b) $z = 80$ mm (far-field region) above a single radiation patch. The contour of the crossed-dipoles element is also plotted here to show the relative position of the element among the field distribution.

of the ACCR FSS are now configured with different sizes (Fig.6(b)). The designed LPSFPA element here can be equivalent to a third-order filtering circuit model shown in Fig. 7. The series L_1C_1 and L_3C_3 branches represent the top and bottom crossed-dipoles resonators of the ACCR FSS, respectively, whereas the parallel L_2C_2 branch represents the middle coupling apertures. The two substrates supporting the ACCR FSS structure are modeled as two transmission lines with length of d and characteristic impedance of $\eta_s = \eta_0/\sqrt{\epsilon_{r1}}$. Both the crossed-dipoles on the top and bottom layers of ACCR FSS operate as half-wavelength resonators for both

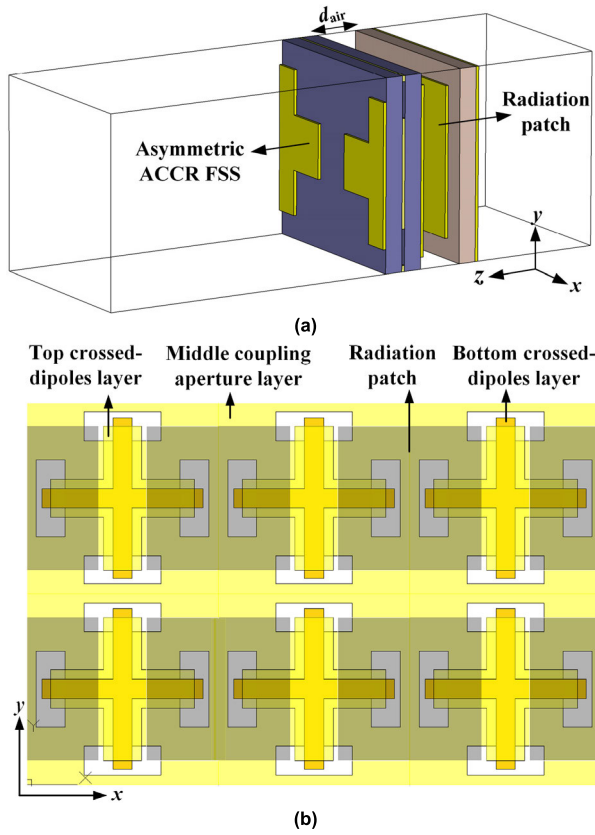


FIGURE 6. (a) 3-D view of a single LPSFPA element. (b) Sketch of relative positions of the radiation patches and the asymmetrical ACCR FSS elements for the LPSFPA.

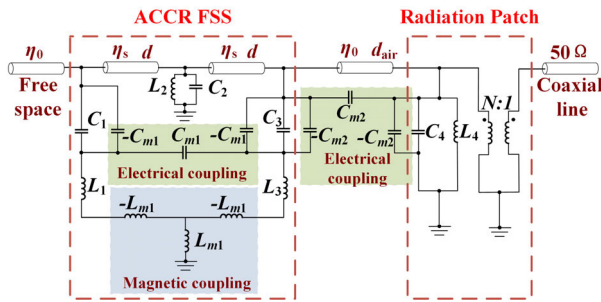


FIGURE 7. Equivalent circuit model of the designed LPSFPA, where all loss is ignored.

x - and y - polarizations. The electrical and magnetic coupling paths between the two crossed-dipoles resonators can be constructed by appropriately designing the coupling apertures in the middle layer. The capacitive coupling is modeled as a “ π ” bridge (C_{m1}) and the inductive coupling is modeled as a “T” bridge (L_{m1}). The radiation patch itself is modeled as the parallel L_4C_4 branch and the feeding coaxial port is modeled as a 50Ω TL. The coupling between the bottom crossed-dipoles resonator and the radiation patch is mainly capacitive and can also be denoted by a “ π ” bridge (C_{m2}). Moreover, in order to describe the impedance transformation effect between the radiation patch and the coaxial feed, an ideal transformer is inserted between the L_4C_4 branch and the 50Ω TL. When the

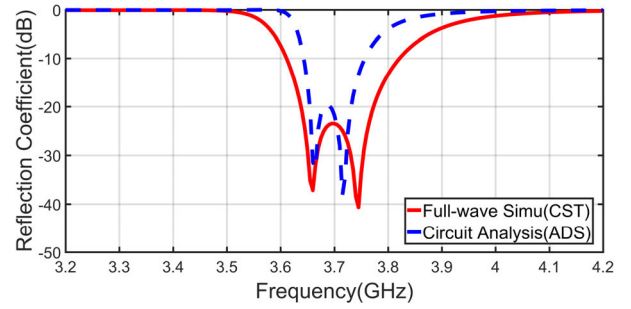


FIGURE 8. Reflection coefficients (full-wave simulation and circuit model analysis) of the symmetric free-standing ACCR FSS with $d = 1.5\text{mm}$, $L_t = 26.2\text{mm}$, $L_b = 26.2\text{mm}$, $W_t = 8\text{mm}$, $W_b = 8\text{mm}$, $L_{bp1} = 21.4\text{mm}$, $L_{bp2} = 13\text{mm}$, $L_{bp3} = 4.8\text{mm}$, $a = 32\text{mm}$, $\epsilon_r = 3$ and $L_1 = 7.35\text{nH}$, $L_2 = 0.269\text{nH}$, $L_3 = 7.35\text{nH}$, $C_1 = 0.2\text{pF}$, $C_2 = 3.17\text{pF}$, $C_3 = 0.2\text{pF}$, $C_{m1} = 0.025\text{pF}$, $L_{m1} = 0\text{nH}$, $\eta_s = 218\Omega$.

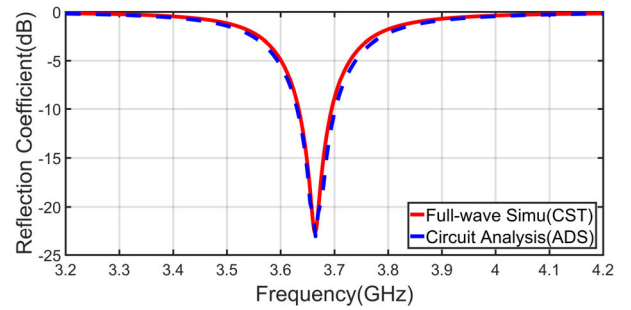


FIGURE 9. Reflection coefficients (full-wave simulation and circuit model analysis) of the free-standing radiation patch array with $L_{ant} = 20.8\text{mm}$, $P = 6.1\text{mm}$ and $L_4 = 0.482\text{nH}$, $C_4 = 3.91\text{pF}$, $N = 0.36$.

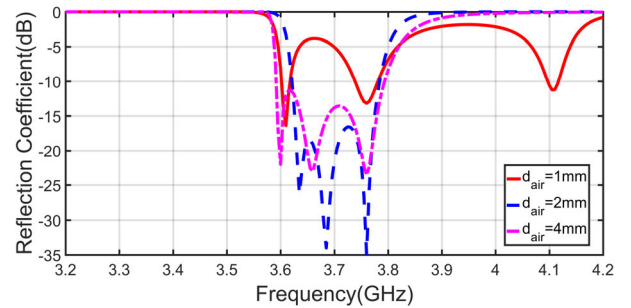


FIGURE 10. Optimized circuit analyzed reflection coefficients of different LPSFPAs with different d_{air} . The optimized circuit parameters for different d_{air} are listed in Table 2.

periodic radiation patch is perfectly matched to the coaxial port at resonance in the free-standing case, the transformation ratio N approximately equals to

$$N = \sqrt{\frac{R_{coax}}{\eta_0}} \approx 0.36, \quad (1)$$

where $R_{coax} = 50\Omega$ is characteristic impedance of the coaxial port and η_0 represents the wave impedance of free space. The free space layers above the LPSFPA and in between the ACCR FSS and the radiation patch array are modeled by transmission lines with characteristic impedance of η_0 . The circuit model given in Fig.7 can help us better analysis the working mechanism of the LPSFPA and guides the design

TABLE 2. The optimized circuit parameters for different d_{air} .

Parameters	Value	Parameters	Value	Parameters	Value
d_{air}	1mm	d_{air}	2mm	d_{air}	4mm
L_1	6.11nH	L_1	6nH	L_1	6.15nH
L_2	0.28nH	L_2	0.28nH	L_2	0.39nH
L_3	10nH	L_3	9.53nH	L_3	9.8nH
L_4	0.457nH	L_4	0.455pF	L_4	0.46nH
C_1	0.22pF	C_1	0.232pF	C_1	0.22pF
C_2	3pF	C_2	3.46pF	C_2	3.1pF
C_3	0.68pF	C_3	0.685pF	C_3	0.68pF
C_4	4.7pF	C_4	4.7pF	C_4	4.4pF
C_{m1}	0.034pF	C_{m1}	0.027pF	C_{m1}	0.047pF
C_{m2}	0.52pF	C_{m2}	0.517pF	C_{m2}	0.528pF
L_{m1}	0nH	L_{m1}	0.1nH	L_{m1}	0pF
N	0.47	N	0.47	N	0.47

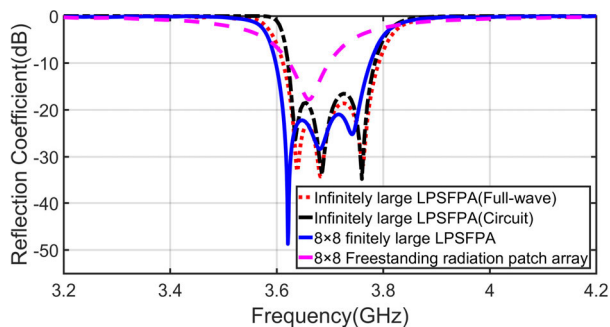


FIGURE 11. Comparison of reflection coefficients of the infinitely large LPSFPA (full-wave simulation and circuit model analysis), the finite 8×8 LPSFPA and the 8×8 freestanding radiation patch array.

TABLE 3. Geometrical dimensions and equivalent circuit parameters of the LPSFPA element.

Parameters	Value	Parameters	Value
L_t	25.7mm	L_1	6.11nH
L_b	28.1mm	L_2	0.283nH
W_t	8mm	L_3	9.5nH
W_b	7mm	L_4	0.457nH
a	32mm	C_1	0.23pF
L_{bp1}	24mm	C_2	3.16pF
L_{bp2}	13mm	C_3	0.687pF
L_{bp3}	3.8mm	C_4	4.7pF
d_{air}	2mm	N	0.47
L_{ant}	21.5mm	C_{m1}	0.026pF
P	4.25mm	C_{m2}	0.518pF
ϵ_{r1}	3	L_{m1}	0.094nH
d	1.5mm	η_s	218 Ω

process. The detailed design process based on the circuit model contains three steps described as follows.

Step I: Design a symmetric free-standing ACCR FSS according to the bandpass filtering requirements such as width of passband and position of transmission zeros. First the rough preliminary values of the relevant equivalent circuit parameters, which is contained in the ACCR FSS part of the circuit model shown in Fig.7, are estimated. Among these parameters, L_2 , L_{m1} are approximated as 0, and L_1C_1 , C_2 , L_3C_3 , C_{m1} are determined via equivalent circuit synthesis according to the rule introduce in [25]. Then the rough preliminary geometries of both cross-dipoles and coupling aperture

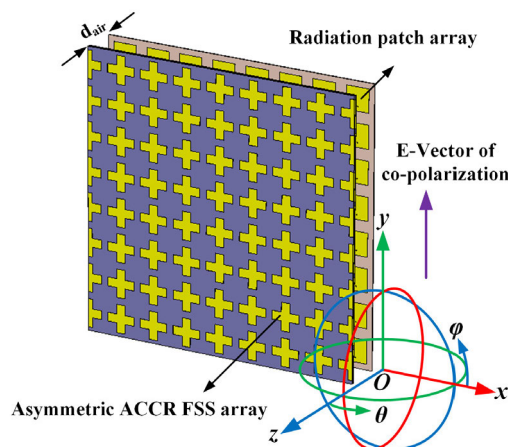


FIGURE 12. Sketch of a finite 8×8 LPSFPA. Note that the $\phi = 90^\circ$ plane (yOz plane) corresponds to E-plane, while the $\phi = 0^\circ$ plane (xOz plane) corresponds to H-plane for normal-beam radiation.

are evaluated through inversion of analytical expressions of the above circuit parameters under the premise that the basic configuration (i.e., multilayer substrate choice and element periodicity) of the FSS is known and fixed. The analytical expressions of the cross-dipoles and coupling aperture are given by [27].

Next the preliminary geometries of the ACCR FSS are carefully adjusted in full-wave simulation software for the purpose of pushing the filtering performance of the FSS close to the requirements. After the fine preliminary geometries of the ACCR FSS are got, the fine preliminary values of circuit parameters (including L_1C_1 , L_2C_2 , L_3C_3 , C_{m1} , L_{m1}) are extracted through curve fitting process based on the simulated scattering performance of the FSS. The reflection coefficients of the fine ACCR FSS from both full-wave simulation and circuit model analysis are compared in Fig. 8. Note in this step, the top and bottom cross-dipoles are regarded as the same, which means $L_1 = L_3$ and $C_1 = C_3$.

Step II: Design the free-standing periodic radiation patch array according to the required operating passband. This step is directly carried out in full-wave simulation software (CST Microwave Studio). After the fine geometries of the radiation patch are got via full-wave simulation, the circuit parameters (L_4C_4) related to the radiation patch are extracted through curve fitting process based on the simulated results. The reflection coefficients of the periodic patch from both full-wave simulation and circuit model analysis are compared in Fig. 9.

Step III: Design the complete LPSFPA. First, a preliminary LPSFPA is constructed by integrating the ACCR FSS and the radiation patch array obtained in the last two steps with certain value of spacing d_{air} and half-periodicity lateral shift along the x-axis. Second, full-wave simulation is carried out for this preliminary LPSFPA and the circuit parameters related to the model shown in Fig.7 are subsequently extracted through curve fitting process with the initial values of L_1C_1 , L_3C_3 , L_2C_2 , C_{m1} , L_{m1} , L_4C_4 set as those obtained

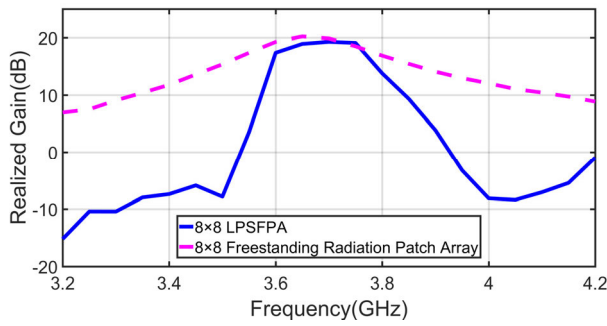


FIGURE 13. Comparison of frequency-dependent co-polarized realized gain along main radiation direction between the 8×8 LPSFPA and the 8×8 freestanding radiation patch array.

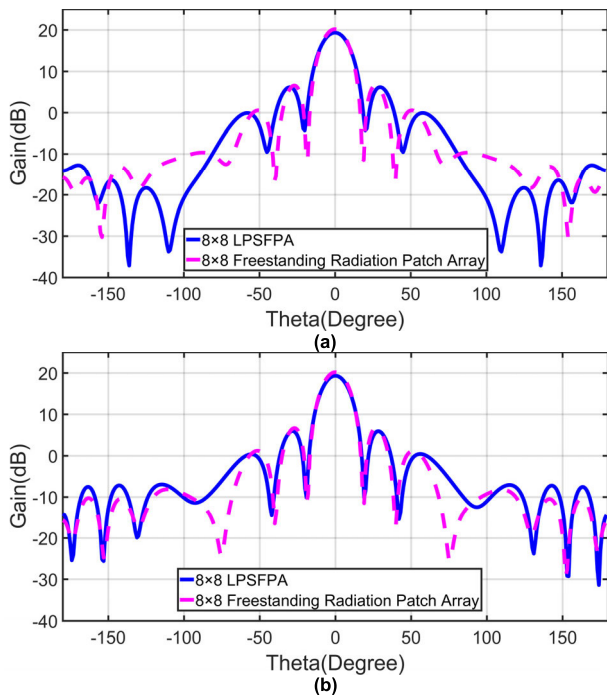


FIGURE 14. Comparison of co-polarized gain patterns between the 8×8 LPSFPA and the 8×8 freestanding radiation patch array at 3.7GHz in (a) H-plane ($\varphi = 0^\circ$) (b) E-plane ($\varphi = 90^\circ$).

in the last two steps, and the initial value of C_{m2} set as 0. Next the equivalent circuit parameters are further tuned to get the optimized circuit analyzed filtering performance of the LPSFPA, where L_1C_1 and L_3C_3 are treated as independently adjustable ($L_1 \neq L_3$ & $C_1 \neq C_3$).

By repeating the above procedures for different choices of d_{air} value, it can be seen from Fig. 10 that the best circuit analyzed filtering performance is achieved when $d_{air} = 2\text{mm}$. Hence, the preliminary LPSFPA with $d_{air} = 2\text{mm}$ is selected as the start point for the final LPSFPA optimization process, where the geometries of LPSFPA element are adjusted by following the tuning directions of the circuit parameters for the corresponding preliminary LPSFPA.

The final geometrical dimensions and the extracted circuit parameters of the optimized LPSFPA element are listed in Table. 3. The full-wave simulated and circuit analyzed

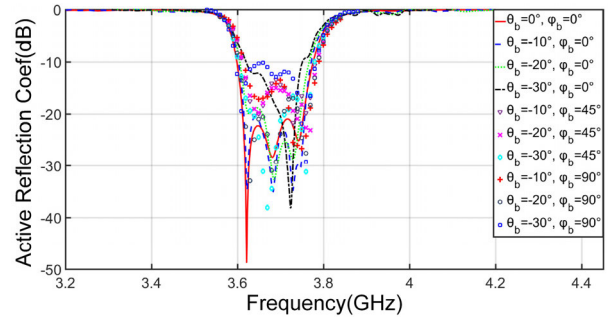


FIGURE 15. Comparison of active reflection coefficients with regard to central element part of the 8×8 LPSFPA with different beam scanning directions.

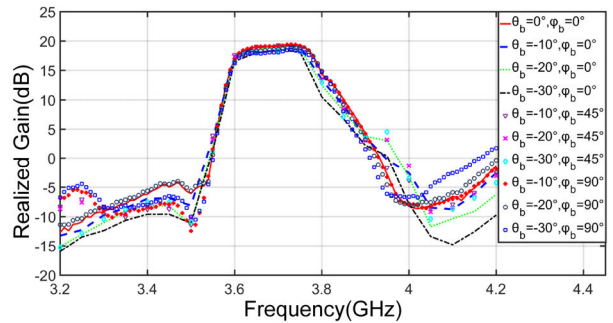


FIGURE 16. Comparison of frequency-dependent co-polarized realized gain along main radiation direction of the 8×8 LPSFPA with different beam scanning directions.

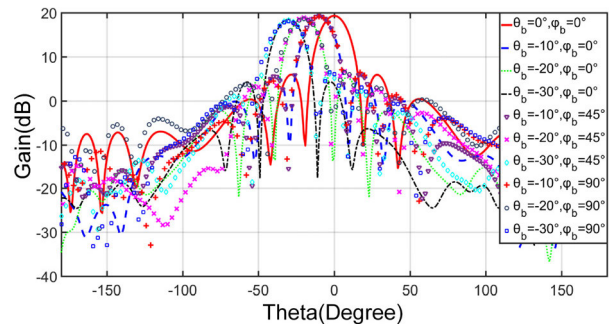


FIGURE 17. Comparison of co-polarized gain patterns of the 8×8 LPSFPA with different beam scanning directions at 3.7GHz. The cutting planes of these 2D radiation patterns are aligned with the azimuth scanning angles ($\varphi_b = 0^\circ, 45^\circ$ and 90° , respectively) of the main beam.

filtering performance are illustrated in Fig. 11 (red and black lines). The two sets of results coincided well with each other. It can be seen that the final LPSFPA has a -10dB impedance bandwidth from 3.61GHz to 3.79GHz and three reflection zeros at 3.64GHz, 3.68GHz and 3.77GHz, respectively.

The above three design steps are associated with infinitely large LPSFPA. To examine the performance of finite array in practice, an 8×8 LPSFPA (as shown in Fig.12) and an 8×8 freestanding radiation patch array as a comparison have also been simulated using time domain solver in CST Microwave Studio. All ports of radiation patch elements are excited with equal-amplitude and equal-phase in the simulation. Note that the dimension and the feeding position of the freestanding radiation patch array are slightly different

from those involved in the finitely large LPSFPA to ensure a consistent operating band for the two finite arrays. The active reflection coefficients, which are associated with the port for either of the four elements located in the central area of the finite arrays are shown in Fig. 11 (blue and pink lines). As shown, the reflection curves of the infinite and finite LPSFPAs agree well with each other except for a slight frequency shift between them. Also, when the reflection curves of the finite arrays with and without the ACCR FSS are compared, it is very obvious that the employment of ACCR FSS leads to an enhanced bandwidth and a much better out-of-band suppression. The same conclusion can be drawn if we compare the frequency responses of forward realized gain of the two finite arrays along the main radiation direction, as shown in Fig. 13. Fig 14 further compares the co-polarized gain patterns of the two finite arrays. A quite good agreement between the two sets of patterns has been achieved except for a slight difference in side lobes and a very small decrease of peak gain identified for the finite LPSFPA.

IV. BEAM SCANNING PROPERTY OF THE LPSFPA

Beam scanning capability is vital for antenna arrays applied in 5G base station. Hence it is necessary to examine the beam scanning properties of the proposed LPSFPA. According to [28], in order to generate a main beam pointing at the required direction, the shift between feeding phases of adjacent array elements should satisfy the following equation

$$\begin{cases} \Delta\psi_x = -\frac{2\pi f}{c}d_x \sin\theta_b \cos\phi_b \\ \Delta\psi_y = -\frac{2\pi f}{c}d_y \sin\theta_b \sin\phi_b \end{cases} \quad (2)$$

where ψ_x and ψ_y are the feeding phase shifts between neighboring LPSFPA elements along the x and y directions, respectively; (d_x, d_y) denote the element periodicity in the x and y directions and (θ_b, ϕ_b) represent the required main beam direction in spherical coordinate system. By controlling the feeding phase of each LPSFPA element, different main beam directions can be achieved in the elevation angle range $\theta_b \in [0^\circ, 30^\circ]$ and azimuth angle range $\phi_b \in [0^\circ, 90^\circ]$ for the 8×8 LPSFPA.

Fig. 15 illustrates the simulation results of active reflection coefficient with regard to central element port and realized gain along the main radiation direction for the 8×8 LPSFPA with various beam scanning angles. As is shown, as the beam scanning angle (either elevation or azimuth) increases, the active reflection coefficient of the LPSFPA gradually deteriorates but still lower than -10 dB in pass-band. Fig. 16 shows that the co-polarized realized gain in pass-band slightly decreases yet still maintain a good out-of-band suppression characteristic as the beam scanning angle increases. Fig. 17 further presents the co-polarized gain patterns of the 8×8 LPSFPA with respect to different beam scanning directions. As shown, there is no significant change in the shape of the radiation pattern when the direction of scanning beam varies.

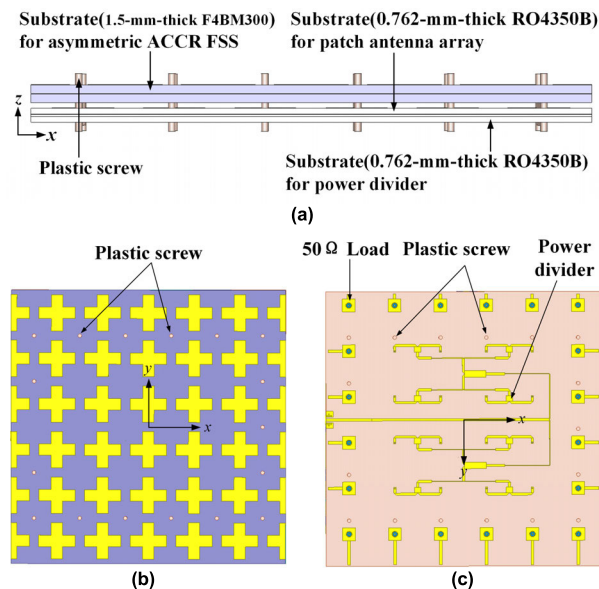


FIGURE 18. Overall structure of the 6×6 LPSFPA with its central 4×4 elements fed by a power divider. (a) Side view. (b) Front view. (c) Back view. The case of equal-phase power divider is shown here as an example.

V. EXPERIMENTAL VERIFICATION AND DISCUSSION

Three LPSFPA samples with different beam scanning angles are fabricated and measured to further verify the proposed design. Owing to our limited experimental conditions, the array scale of the fabricated LPSFPA samples is reduced to 6×6 . Three additional microstrip power dividers with equal-amplitude and 1D-gradient-phase outputs are designed as the feeding networks for the three LPSFPAs, respectively. The output phase steps of the three power dividers are $0^\circ, 35^\circ, 70^\circ$, respectively, corresponding to the scanning directions of $\phi_b = 90$ and $\theta_b = 0^\circ, 15^\circ$ and 30° , respectively. To suppress the edge effect of finite array, the 20 edge and corner elements of the three LPSFPA samples are all terminated with $50\text{-}\Omega$ load and only the central 4×4 elements are excited with certain power divider. The overall structure of the LPSFPA fed by power divider is illustrated in Fig. 18. The fabrication process of the three LPSFPA samples is described below. First, using the art of multilayer printed circuit board (PCB), the designed asymmetric ACCR FSS is fabricated with two 1.5-mm-thick F4BM300 copper-clad laminates, which are bonded together using a 0.1-mm-thick FR4 prepreg. Three identical FSS samples are produced in this step. Second, the three different power dividers and the designed radiation patch arrays are fabricated using PCB art with 0.762-mm-thick RO4350B laminates. Three identical radiation patch arrays are produced in this step. Next, each of the three power dividers is bonded ground-to-ground by a 0.2-mm-thick RO4450F prepreg to one radiation patch array. Each of the 16 central radiation patch elements is electrically connected to certain output port of power divider through a metalized via. Finally, each of the three LPSFPA samples is assembled by connecting and fixing the board bearing the asymmetric ACCR FSS and the board carrying certain

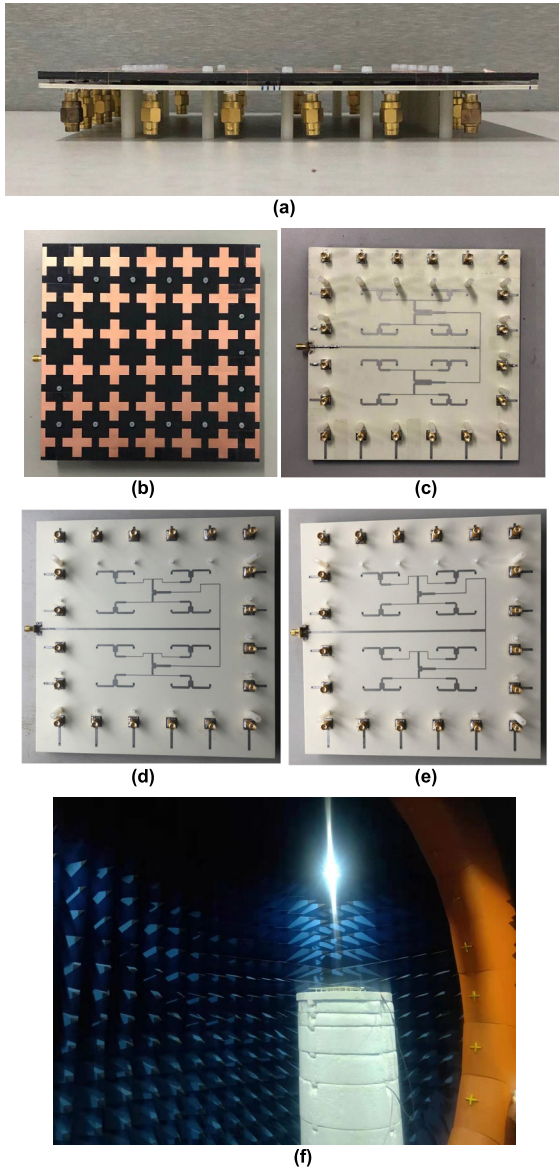


FIGURE 19. (a) Side view, (b) front view and (c)-(e) back view of the fabricated LPSFPA prototype fed by power divider with (c)0°, (d)35° and (e)70° output phase steps. (f) Scene of prototype measurement using spherical near field testing platform in anechoic chamber.

power divider and the radiation patch array through plastic screws. The realistic view of the finial fabricated LPSFPAs is given in Fig. 19. In order to make a comparison, an ordinary normal-beam 6×6 radiation patch array without FSS covering (control array) is also fabricated. It is fed by an equal-phase power dividing network with regard to the central 4×4 elements.

The reflection coefficients of the fabricated LPSFPA samples and the control array are measured using Keysight handheld analyzer (N9918A) and shown in Fig. 20. We remark that, with the existence of power divider, the active reflection coefficient with respect to each LPSFPA element is not available in experiment. Instead, only the total reflection coefficient with respect to the entire array

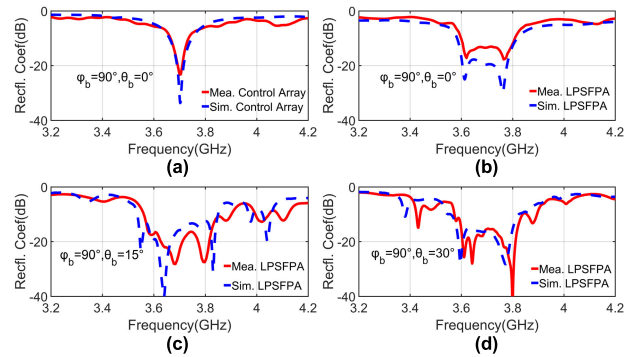


FIGURE 20. Comparison of measured and simulated reflection coefficients of fabricated samples with different main beam directions. (a) Control array @ $\theta_b = 0^\circ$, $\varphi_b = 90^\circ$, (b) LPSFPA @ $\theta_b = 0^\circ$, $\varphi_b = 90^\circ$, (c) LPSFPA @ $\theta_b = 15^\circ$, $\varphi_b = 90^\circ$, (d) LPSFPA @ $\theta_b = 30^\circ$, $\varphi_b = 90^\circ$.

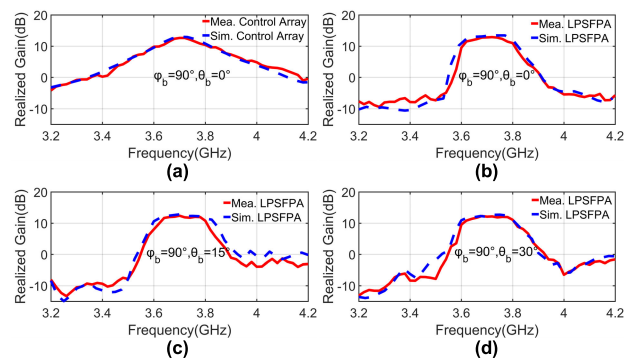


FIGURE 21. Comparison of measured and simulated frequency-dependent peak co-polarized realized gain of fabricated samples with different main beam directions. (a) Control array @ $\theta_b = 0^\circ$, $\varphi_b = 90^\circ$, (b) LPSFPA @ $\theta_b = 0^\circ$, $\varphi_b = 90^\circ$, (c) LPSFPA @ $\theta_b = 15^\circ$, $\varphi_b = 90^\circ$, (d) LPSFPA @ $\theta_b = 30^\circ$, $\varphi_b = 90^\circ$.

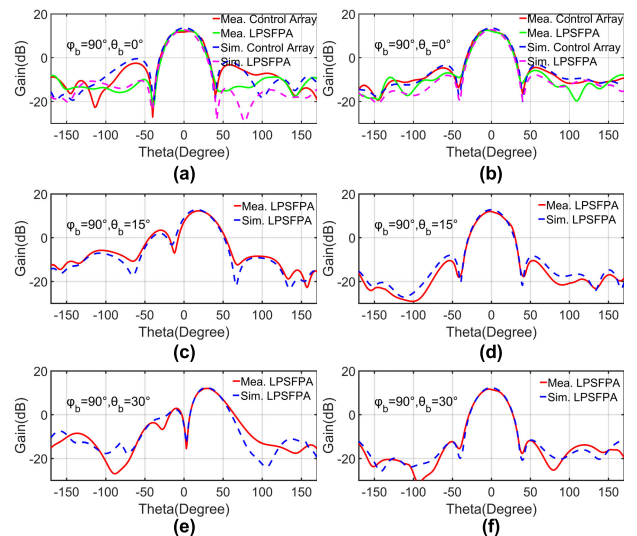


FIGURE 22. Comparison of measured and simulated co-polarized gain patterns of fabricated samples with main beam directions of (a)(b) $\theta_b = 0^\circ$, $\varphi_b = 90^\circ$, (c)(d) $\theta_b = 15^\circ$, $\varphi_b = 90^\circ$ and (e)(f) $\theta_b = 30^\circ$, $\varphi_b = 90^\circ$ at 3.7GHz in (a)(c) E-plane and (b)(d)(f) H-plane. For H-plane patterns, the cutting plane is aligned with the elevation scanning angles (θ_b) of the main beam.

and referenced at the feeding port of power divider can be measured. The radiation performances of the samples,

TABLE 4. Comparison with previous spatial filtering cases.

Reference	Antenna type	Number of metallic layers of FSS	Distance between antenna and FSS	Shape factor (BW ^{20dB} /BW ^{3dB})	-10dB BW (Reflection coefficient)	Stability of angular-scan performance	
						Elevation angle	Azimuth angle
[18]	Patch	2	0.1λ _g	5.7	< 2% @ 10.5GHz	15°	/
[19]	Patch	2	0.1λ _g	5	4.8% @ 10.5GHz	20°	/
[20]	Patch	3	0.062λ _g	4	3.19% @ 2.1GHz	15°	/
[23]	Dipole	5	0.5λ _g	About 2	27% @ 4.5GHz	< 45°	arbitrary
[24]	Patch	1	0.37λ _g	About 3.5	/	30°	/
Our work	Patch	3	0.025λ _g	2.1	5.4% @3.7GHz	30°	arbitrary

including the peak co-polarized realized gain along the main radiation directions and the 2D co-polarized gain patterns are measured using spherical near field testing platform in anechoic chamber and shown in Fig. 21 and Fig. 22. Apparently, as shown in Fig.20(a)-(b) and Fig. 21(a)-(b), the normal-beam LPSFPA sample can achieve an improved impedance bandwidth and an enhanced out-of-band suppression compared with the control array. Specifically, the measured -10dB impedance bandwidth is from 3.6GHz to 3.82GHz; the measured out-of-band suppression level is more than 19 dB in the lower band-edge from 3.2 GHz to 3.5 GHz and more than 17 dB in the upper band-edge from 3.9 GHz to 4.2 GHz. It should be emphasized that the fabricated LPSFPA appears not to be competitive in terms of out-of-band rejection when compared with the 8 × 8 LPSFPA shown in Fig. 12. This is mainly due to the reduced scale of the fabricated samples. From the measured results shown in Fig.20(c)-(d) and Fig.21(c)-(d), the spatial filtering characteristic of the oblique-beam LPSFPA samples is also experimentally verified. Specifically, compared with the normal-beam sample, the impedance bandwidth of the oblique-beam samples varies slightly and still covers the band from 3.6GHz to 3.8 GHz; the out-of-band suppression of the oblique-beam samples slightly deteriorates, but still maintains a good level. Fig. 22 further illustrates the beam scanning capability of the fabricated LPSFPAs. From Fig. 22(a)-(b), it is found that the main beam shape of the normal-beam LPSFPA is in good agreement with that of the control array without any significant change. It should be noted that the first side lobes of the LPSFPA in both E- and H-planes are lower than those of the control array. This is mainly attributed to the suppression of large angle radiation by ACCR FSS. As shown in Fig. 22(a)-(b), the first side lobes of the control array appear around ±60°, which corresponds to a large oblique incident angle with respect to the ACCR FSS and hence a significant attenuation in passband of the ACCR FSS. In comparison, as shown in Fig. 14, the first side lobes of the 8 × 8 radiation patch array appear around ±30° and the passband attenuation of the ACCR FSS is not obvious at this small angle of oblique incidence. Hence the side lobes of the 8 × 8 LPSFPA are just slightly lower than those of the freestanding radiation patch array.

The simulated performances of the fabricated samples are also contained in Figs. 20 to 22 for comparison. It's found that the measured impedance bandwidths and realized gains of the LPSFPA samples are slightly different from the simulated results. The impedance bandwidth difference is mainly due to the assembly error of distance between the radiation patch array and the ACCR FSS, which causes change of mutual coupling between them. Also, owing to the fabrication errors of feeding network and the imperfect planeness of PCB, the measured realized gains of the LPSFPA samples are lower than the simulated ones. Specifically, for the normal-beam case shown in Fig.21(a)-(b), the measured peak realized gain of the LPSFPA and the control array are 13.4 dB and 12.6 dB at 3.7GHz, which are 0.7 dB and 0.9 dB lower than the simulated counterparts, respectively. This phenomenon can also be observed in the oblique-beam cases shown in Fig.21(c)-(d).

In order to better exhibit the superiority of the proposed design, Table 4 shows the comparison between our design and other existing spatial filtering designs. It is shown that the proposed LPSFPA design has more compact volume, better beam scanning stability and better out-of-band rejection. Considering these favorable spatial filtering characteristics, the proposed LPSFPA is a good candidate for potential Massive MIMO base station applications.

VI. CONCLUSION

This paper proposes a low-profile spatial filtering patch antenna array (LPSFPA) by combining an asymmetric ACCR FSS and a radiation patch array into an integral structure with a thickness of 0.07λ₀. It has been verified through both simulation and experiment that the LPSFPA features greatly improved out-of-band suppression at double band-edges compared with the ordinary patch antenna array. Moreover, its filtering performance and radiation performances are stable when its radiation beam is scanning in the elevation angle range of 0 to 30° with arbitrary azimuth angle. Replacement of ordinary patch antenna array by the proposed LPSFPA can significantly ease the requirement of discrete bandpass filters in RF channels. Hence the proposed LPSFPA is promising for applications in RF front-end of Massive MIMO base stations. Further research on the LPSFPA with respect to issues such

as controlling of transmission zero positions, tuning of the impedance bandwidth, and extension of dual-polarization is under progress.

REFERENCES

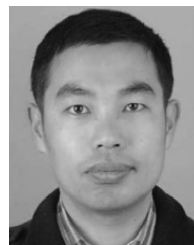
- [1] J. Zuo, X. Chen, G. Han, L. Li, and W. Zhang, "An integrated approach to RF antenna-filter co-design," *IEEE Antennas Wireless Propag. Lett.*, vol. 8, pp. 141–144, 2009.
- [2] Y. Yusuf, H. Cheng, and X. Gong, "A seamless integration of 3-D vertical filters with highly efficient slot antennas," *IEEE Trans. Antennas Propag.*, vol. 59, no. 11, pp. 4016–4022, Nov. 2011.
- [3] C.-T. Chuang and S.-J. Chung, "Synthesis and design of a new printed filtering antenna," *IEEE Trans. Antennas Propag.*, vol. 59, no. 3, pp. 1036–1042, Mar. 2011.
- [4] C.-K. Lin and S.-J. Chung, "A compact filtering microstrip antenna with quasi-elliptic broadside antenna gain response," *IEEE Antennas Wireless Propag. Lett.*, vol. 10, pp. 381–384, 2011.
- [5] X. Chen, F. Zhao, L. Yan, and W. Zhang, "A compact filtering antenna with flat gain response within the passband," *IEEE Antennas Wireless Propag. Lett.*, vol. 12, pp. 857–860, 2013.
- [6] T. Li and X. Gong, "Vertical integration of high- Q filter with circularly polarized patch antenna with enhanced impedance-axial ratio bandwidth," *IEEE Trans. Microw. Theory Techn.*, vol. 66, no. 6, pp. 3119–3128, Jun. 2018.
- [7] B. Zhang and Q. Xue, "Filtering antenna with high selectivity using multiple coupling paths from source/load to resonators," *IEEE Trans. Antennas Propag.*, vol. 66, no. 8, pp. 4320–4325, Aug. 2018.
- [8] Y. Li, Z. Zhao, Z. Tang, and Y. Yin, "Differentially fed, dual-band dual-polarized filtering antenna with high selectivity for 5G sub-6 GHz base station applications," *IEEE Trans. Antennas Propag.*, vol. 68, no. 4, pp. 3231–3236, Apr. 2020.
- [9] X. Y. Zhang, Y. Zhang, Y.-M. Pan, and W. Duan, "Low-profile dual-band filtering patch antenna and its application to LTE MIMO system," *IEEE Trans. Antennas Propag.*, vol. 65, no. 1, pp. 103–113, Jan. 2017.
- [10] X. Y. Zhang, W. Duan, and Y.-M. Pan, "High-gain filtering patch antenna without extra circuit," *IEEE Trans. Antennas Propag.*, vol. 63, no. 12, pp. 5883–5888, Dec. 2015.
- [11] Y. Zhang, Y. Zhang, D. Li, Z. Niu, and Y. Fan, "Dual-polarized low-profile filtering patch antenna without extra circuit," *IEEE Access*, vol. 7, pp. 106011–106018, 2019.
- [12] J.-F. Qian, F.-C. Chen, Q.-X. Chu, Q. Xue, and M. J. Lancaster, "A novel electric and magnetic gap-coupled broadband patch antenna with improved selectivity and its application in MIMO system," *IEEE Trans. Antennas Propag.*, vol. 66, no. 10, pp. 5625–5629, Oct. 2018.
- [13] J. Y. Jin, S. Liao, and Q. Xue, "Design of filtering-radiating patch antennas with tunable radiation nulls for high selectivity," *IEEE Trans. Antennas Propag.*, vol. 66, no. 4, pp. 2125–2130, Apr. 2018.
- [14] J.-F. Li, Z. N. Chen, D.-L. Wu, G. Zhang, and Y.-J. Wu, "Dual-beam filtering patch antennas for wireless communication application," *IEEE Trans. Antennas Propag.*, vol. 66, no. 7, pp. 3730–3734, Jul. 2018.
- [15] M. Xun, W. Yang, W. Feng, Y. Zhang, Q. Xue, and W. Che, "A differentially fed dual-polarized filtering patch antenna with good stopband suppression," *IEEE Trans. Circuits Syst. II, Exp. Briefs*, vol. 68, no. 4, pp. 1228–1232, Apr. 2021.
- [16] Y. F. Cao, Y. F. Wu, Y.-M. Pan, and X. Y. Zhang, "A method of generating radiation nulls utilizing inherent resonance modes for dual-polarized filtering dipole antenna design," *IEEE Trans. Antennas Propag.*, vol. 68, no. 8, pp. 6413–6418, Aug. 2020.
- [17] Y. M. Pan, P. F. Hu, X. Y. Zhang, and S. Y. Zheng, "A low-profile high-gain and wideband filtering antenna with metasurface," *IEEE Trans. Antennas Propag.*, vol. 64, no. 5, pp. 2010–2016, May 2016.
- [18] W. Yang, S. Chen, Q. Xue, W. Che, G. Shen, and W. Feng, "Novel filtering method based on metasurface antenna and its application for wideband high-gain filtering antenna with low profile," *IEEE Trans. Antennas Propag.*, vol. 67, no. 3, pp. 1535–1544, Mar. 2019.
- [19] F. Bayatpur and K. Sarabandi, "Miniaturized FSS and patch antenna array coupling for angle-independent, high-order spatial filtering," *IEEE Microw. Wireless Compon. Lett.*, vol. 20, no. 2, pp. 79–81, Feb. 2010.
- [20] F. Bayatpur and K. Sarabandi, "A metamaterial-based spatial filter for phased-array applications," in *Proc. IEEE Antennas Propag. Soc. Int. Symp.*, Charleston, SC, USA, Jun. 2009, pp. 1–4.
- [21] S. M. A. M. H. Abadi, M. Li, and N. Behdad, "Harmonic-suppressed miniaturized-element frequency selective surfaces with higher order bandpass responses," *IEEE Trans. Antennas Propag.*, vol. 62, no. 5, pp. 2562–2571, May 2014.
- [22] X. Yang, H. Luyen, S. Xu, and N. Behdad, "Design method for low-profile, harmonic-suppressed filter-antennas using miniaturized-element frequency selective surfaces," *IEEE Antennas Wireless Propag. Lett.*, vol. 18, no. 3, pp. 427–431, Mar. 2019.
- [23] C. Yepes, D. Cavallo, E. Gandini, S. Monni, A. Neto, and F. E. van Vliet, "Angularly stable frequency selective surface combined with a wide-scan phased array," *IEEE Trans. Antennas Propag.*, vol. 66, no. 2, pp. 1046–1051, Feb. 2018.
- [24] Y.-P. Hong, I.-J. Hwang, D.-J. Yun, D.-J. Lee, and I.-H. Lee, "Design of single-layer metasurface filter by conformational space annealing algorithm for 5G mm-wave communications," *IEEE Access*, vol. 9, pp. 29764–29774, 2021.
- [25] D. S. Wang, P. Zhao, and C. H. Chan, "Design and analysis of a high-selectivity frequency-selective surface at 60 GHz," *IEEE Trans. Microw. Theory Techn.*, vol. 64, no. 6, pp. 1694–1703, Jun. 2016.
- [26] R.-X. Liao, S.-W. Wong, Y. Li, J. Y. Lin, B.-Y. Liu, F.-C. Chen, and Z. Quan, "Quasi-elliptic bandpass frequency selective surface based on coupled stubs-loaded ring resonators," *IEEE Access*, vol. 8, pp. 113675–113682, 2020.
- [27] N. Marcuvitz, *Waveguide Handbook*. New York, NY, USA: McGraw-Hill, 1951.
- [28] W. L. Stutzman and G. A. Thiele, *Antenna Theory and Design*. Hoboken, NJ, USA: Wiley, 1998.



YE LI was born in Changzhou, China, in 1994. He received the B.E. degree in electronic information engineering from the Nanjing Institute of Technology, Nanjing, China, in 2018, and the M.E. degree in electronic and communication engineering from Soochow University, Suzhou, China, in 2021. In 2023, he joined the CCTEG Changzhou Research Institute, Changzhou. His research interests include frequency selective surfaces, spatial filtering, and base station antenna design.



XURAN NIE was born in Jiyuan, China, in 1997. He received the B.E. degree in electronic information engineering from Henan Normal University, Xixiang, China, in 2020. He is currently pursuing the M.E. degree in electronic and communication engineering with Soochow University, Suzhou, China. His research interests include filtering antenna and base station antenna design.



XINMI YANG (Member, IEEE) was born in Suzhou, Jiangsu, China, in March 1982. He received the B.S. and Ph.D. degrees from the School of Information Science and Engineering, Southeast University, Nanjing, China, in 2005 and 2010, respectively. In November 2010, he joined the School of Electronics and Information Engineering, Soochow University, Suzhou, China, and he has been an Associate Professor since July 2014. Since 2021, he has been with the School of

Electronic Engineering, Yangtze Delta Region Institute (Huzhou), University of Electronic Science and Technology of China, as a Research Fellow. He has authored and co-authored more than 50 technical journal articles. He co-edited the book *Metamaterials - Beyond Crystals, Noncrystals, and Quasicrystals* (CRC Press, June 2016) and he is the author of two book chapters. His current research interests include metamaterials, metasurfaces, and their applications on antennas and microwave engineering.



CHANGRONG LIU (Member, IEEE) was born in Jiangsu, China, in 1986. He received the B.E. degree in electronic information science and technology and the M.E. and Ph.D. degrees in radio physics from the University of Electronic Science and Technology of China, Chengdu, China, in 2008, 2011, and 2015, respectively. From March 2010 to March 2011, he was a Visiting Student with the Department of Electrical and Computer Engineering, NUS, Singapore, where he was a Visiting Scholar, from August 2012 to August 2014. In August 2015, he joined Soochow University, Suzhou, China, as an Associate Professor. He has authored/coauthored over 50 technical journal articles and conference papers. His main research interests include LTCC-based millimeter-wave antenna array design, circularly polarized beam-steering antenna array, and implantable antennas for biomedical applications, including wireless data telemetry and power transfer. He was a recipient of the Best Student Paper Award from the National Conference on Microwave and Millimeter Waves held in Qingdao, China, in 2011. He was a co-recipient of the Best Poster Award from the International Conference on Wearable, in 2014, and the Implantable Body Sensor Networks held in Zürich, Switzerland, in 2014.

Supervisor in July 2009 and December 2011, respectively. From September 2011 to September 2012, he was a Postdoctoral Researcher with the Department of Electromagnetic Engineering, Royal Institute of Technology, Stockholm, Sweden. He is currently a Full Professor with UESTC. He has authored more than ten patents, more than 60 scientific journal articles, and has presented more than 60 conference papers. His research interests include microwave/millimeter-wave circuits, antennas, and microwave power transmission and applications.



XIANQI LIN (Senior Member, IEEE) was born in Zhejiang, China, in July 1980. He received the B.S. degree in electronic engineering from the University of Electronic Science and Technology of China (UESTC), Chengdu, China, in 2003, and the Ph.D. degree in electromagnetic and microwave technology from Southeast University, Nanjing, China, in 2008. He joined the Department of Microwave Engineering, UESTC, in August 2008, and he became an Associate Professor and a Ph.D.

KEMENG HUANG, photograph and biography not available at the time of publication.

...